Clay, P.L., et al., 2023, Extreme serpentinization and desulfurization in an early Earth setting: Geology, https://doi.org/10.1130/G51030.1.

Supplemental Material

Text. Detailed Geological Setting and Supplementary Interpretation, as well as Methodology.

Table S1 Nickel-rich minerals typical of the Bon Accord Ni oxide deposit.

Table S2. (A) Major element composition (wt.% oxide) of bulk Bon Accord and trevorite and silicate concentrates. Data are recalculated to a normalized anhydrous composition. An average bulk composition (n = 2) with 2 standard deviation (S.D.) is calculated. (B) Trace element composition (ppm) of bulk Bon Accord and trevorite and silicate concentrates measured by solution ICP-MS.

Table S3. Potassium, Ca, Ba and halogen abundances in Bon Accord trevorite (12.2 mg) and bulk rock (5.1 mg) determined by NI-NGMS. Potassium, Ca, Ba and Cl are given in ppm and Br and I are given in ppb. All ratios are by weight. Uncertainties are 1σ, and are given in the units of the last significant figure(s).

Table S4. Noble gas data for a 101.60 mg sample of Bon Accord. Uncertainties are 1σ, and are given in the units of the last significant figure(s). Helium, Ne and Ar concentrations are units of 10^{-8} cm^3 STP g^{-1} and Kr and Xe are in units of 10^{-10} cm^3 STP g^{-1}.

Table S5. Highly-siderophile element (HSE) abundance data are given in ppm. $^{187}Re/^{188}Os$ and $^{187}Os/^{188}Os$ data have a 2 standard error (S.E.).

Table S6. Zinc isotopic data for three Bon Accord (bulk) samples.

Table S7 Serpentinization and desulfurization reaction parameters and mass balance for the Bon Accord Ni oxide deposit.

Figure S1. Schematic (not to scale) north-south oriented cross section through the stratigraphy ~1 km southeast of the Bon Accord Ni oxide deposit, which was sited at the same location in the sequence as the trevorite-nimite schists in the hanging wall immediately above the Ni-sulfide mineralization (shown in red).

Figure S2. Mineralogy and microstructure of the Bon Accord trevorite deposit.

Figure S3. Br/Cl and I/Cl ratios of Bon Accord in relation to reference compositions for modern seawater and fields for komatiites, serpentinites, marine pore fluids, mantle and modern hydrothermal vent fluids (Br/Cl range only shown in vertical band in (C)).

Figure S4. Bon Accord zinc isotope systematics.

Supplementary Information for: Extreme serpentinization and desulfurization in an early Earth setting

Patricia L. Clay, James M.D. Day, Henner Busemann, Pierre Bonnand, Ray Burgess, Richard A. Hornsey, Richard D. Ash, Frédéric Moynier and Brian O'Driscoll

- Supplementary Text: Detailed Geological Setting and Methods
- Tables S-1 to S-7
- Figures S1-S4
- Supplementary Information References

Supplementary Text

Detailed Geological Setting and Supplementary Interpretation

The Bon Accord Ni oxide body was located at the margin of the northernmost Barberton Greenstone Belt (BGB; **Fig. 1, main manuscript**), in the immediate hanging wall of a granitic gneiss dome referred to as the Stentor Pluton. It consisted of an elliptical body ~6 m^3 in volume and was discovered more than a century ago. It was completely excavated soon after this due to its high Ni content (up to 35% bulk rock; Trevor, 1920). However, it proved too refractory to smelt and was discarded. Little material remains today, but the sample studied here comes from the original Bon Accord body, and was provided by Professor Grant Cawthorn, University of the Witwatersrand (South Africa; see also O'Driscoll et al. 2014).

In the northern region of the BGB, the metamorphic grade locally increases across a high strain zone recording upper greenschist to upper amphibolite facies conditions, toward the Stentor granitoid, with the higher grade of metamorphism locally affecting the BGB rocks closest to the greenstone-granitoid contact (Viljoen and Viljoen, 1969; Lowe, 1999; Dziggel et al., 2010, Anhaeusser, 2019). Approximately 10 km along strike from Bon Accord, at the New Consort gold mine, the bulk of the mineralization has been shown to be associated with a steeply southward-dipping syn-magmatic shear zone system (Dziggel et al., 2010). The sequence of rocks at Bon Accord has previously been assigned to the Tjakastad Subgroup of the Onverwacht Group (Keenan, 1986; Tredoux et al., 1989), but there is uncertainty in this due to the metamorphism and high degree of structural complexity of the rocks, and it is possible that a higher stratigraphic level is represented, i.e., the Weltevreden Formation of the Onverwacht Group (Anhaeusser, 1986; 2019). Close (<500 m) to the contact with the Stentor granitoid, the Bon Accord sequence broadly comprises a package of schistose metasediments and massive cherts (the latter containing lenticular serpentinite bodies), separated by a steeply-southward dipping low angle shear zone from a thick package of grey serpentinite (**Fig. S-1**). The shear zone is up to 30 cm thick and composed of talc schist. In the shear zone footwall, a complex sequence of sulfide-mineralized chert and massive sulfide ore occurs, whilst in the hanging wall, a number of discontinuous trevorite-nimite schist bodies (with disseminated sulfide mineralization) are present. The Bon Accord Ni-oxide body, as well as other oxide (e.g., hematite)-rich bodies, occur in the hanging wall of the shear zone (Keenan, 1986), at the same stratigraphic level as the trevorite-nimite schists.

The northern margin of the BGB was subjected to a complex series of tectonometamorphic events following deposition and magma emplacement, lasting up to 200 Ma in duration, and largely associated with the emplacement and exhumation of mid-crustal gneiss domes such as the Stentor and Kaap Valley Plutons (Dziggel et al., 2010; Anhaeusser, 2019). The close spatial association of the Bon Accord trevorite assemblage with a sub-vertical low angle shear zone allows the approximate tectonic context for the metasomatism to be surmised. Such shear zones, also characterized by a sinistral strike-slip component of motion, are recognized at the New Consort mine ~10 km to the east, where they are associated with the onset of gold mineralization (Dziggel et al., 2010). It is worth noting in this context that trevorite aggregates in the Bon Accord sample studied here have forms that suggest sinistral shearing (**Fig. 2, main manuscript; Fig. S-2a**). Furthermore, the microstructure of the trevorite aggregates indicates polyphase deformation

and recrystallization (**Fig. 2**). The occurrence of the Bon Accord Ni-oxide body in the immediate hanging wall of the shear zone (**Fig. S-1**) accounts for the deformation-related microstructures.

Although there is considerable uncertainty in relating the Bon Accord deformation and metamorphism to the regional tectonometamorphic picture with the evidence to hand, the Re-Os isotope systematics are supportive of formation of the Bon Accord oxide body at ~3.2−3.3 Ga, although the discordant behavior suggests some degree of disturbance (**Fig. 3b, main manuscript**); γOs - the percent deviation of $^{187}Os/^{188}Os$ at the time of crystallization from the chondritic reference – has values of ~-6 to +1 at 3.5 Ga or +2 to +6 at 3.2 Ga. However, given that the HSE are mainly sited in the trevorite-hosted HSE-bearing inclusions, these data probably reflect the approximate timing of trevorite crystallization and rule out post-Archean crystallization. The slight relative enrichment of Ru, Pt, Pd and Re over Os and Ir might reflect a degree of magmatic differentiation during sulfide formation. The QEMSCAN image reveals the patchy but pervasive growth of liebenbergite in areas of nèpouite groundmass throughout the Bon Accord sample (**Fig. 2, main manuscript**) – the liebenbergite is interpreted here as reflecting relatively late-stage dehydration of népouite. The northern margin of the BGB was locally subjected to amphibolite facies conditions because of proximity to the granitoids, given the small distance between Bon Accord and the Stentor Pluton, dehydration was probably a contact metamorphic effect. The fact that the nimite-bearing micro-shear bands crosscut these népouite patches serves to indicate that the Bon Accord oxide body experienced a polymetamorphic history, reflective of the wider northern BGB.

Methods

QEMSCAN Mineral Mapping

The modal mineralogy of Bon Accord was calculated using the FEI QEMSCAN modal analysis at 10 µm and 1 µm pixel resolution (**Fig. 2 in main manuscript**).

Major and Trace Element Analysis

Major and trace element abundances were done on homogeneous powders using standard techniques developed at the Scripps Isotope Geochemistry Laboratory (SIGL). Approximately 50 mg of sample powder was dissolved within closed Teflon vials in Teflon-distilled 27.5M HF (4 mL) and 15.7M HNO_3 (1 mL) for >72 h on a hotplate at 150°C, along with total procedural blanks and terrestrial basalt and andesite standards (BHVO-2, BCR-2, BIR-1a, AGV-2). The 50 mg powder aliquot was taken from a larger homogenized sample powder. Acid attack led to complete dissolution of rock samples, generating clear solutions, with no remaining solid material. Samples were sequentially dried and taken up in concentrated HNO_3 to destroy fluorides, followed by doping with indium to monitor instrumental drift during analysis, and then diluted to a factor of 5,000. Trace-element abundances were determined using a ThermoScientific iCAP Qc quadrupole inductively coupled plasma mass spectrometer (ICP-MS) and all reported data are blank-corrected and >10× limit of quantification. Long-term reproducibility of abundance data based on long-term analytical campaigns at the SIGL is better than 6% for most elements, except for Mo, Te and Se (>10%; Day et al., 2018).

Major element abundances were determined on the same solutions used for trace element abundance determination, using a dilution factor of 50,000. Major-element abundances were determined using a ThermoScientific iCAP Qc q ICP-MS. For major-elements, Si was derived by difference, with reproducibility of other elements measured on the BHVO-2 reference material being better than 3%, except Na_2O (7.1%). The ICP-MS method is ideal for determination of major- and trace-elements in fresh samples with minimal alteration and/or for which limited sample mass (less than 2 g) is available for study, such as the Bon Accord material. A caveat is that limited sample masses can lead to a mode-effect, where non-representative volumes of rock are chosen, resulting in greater variability in chemical measurements, as described in the discussion.

Halogen Abundance Analysis

Halogens act as important ligands for mineralization and are powerful tracers of fluid source and evolution (e.g., Kendrick et al., 2013). Halogen (Cl, Br and I), Ca, K and Ba abundances were determined by the neutron irradiation noble gas mass spectrometry method (NI−NGMS) detailed in

Ruziè-Hamilton et al. (2016). Chlorine Br, and I are converted into noble gas isotopes $^{38}Ar_{Cl}$, $^{80,82}Kr_{Br}$ and $^{128}Xe_{I}$ through neutron bombardment. Al−foil wrapped samples were encapsulated under vacuum in SiO_2−glass tubing before packing in Al canisters for a 24 h continuous irradiation at the Petten Reactor, Netherlands ("MN13"). The neutron fluence was monitored with $^{40}Ar-^{39}Ar$ and I−Xe geochronological standard minerals "Hb3Gr" hornblende (1080.4 ± 1.1 Ma; Renne et al., 2010) and enstatite separated from the Shallowater aubrite ($^{129}I/^{127}I_{initial}$ = 1.072 ×10^{-4}; Brazzle et al., 1999). Scapolite minerals ("BB−1", "BB−2" and "SP") were monitored for epithermal neutron fluence (Ruzié-Hamilton et al., 2016).

Two Bon Accord samples (a 12.2 mg trevorite fraction and a 5.1 mg bulk fraction) were heated incrementally with a Nd:YAG infrared laser on the static vacuum MS1 mass spectrometer at the University of Manchester. Argon isotopes were measured using a Faraday detector (10^{11} Ohm resistor) and Kr and Xe isotopes were measured with a channeltron electron multiplier. Gases were purified on hot and room temperature SAES® NP10 getters for 20 minutes prior to analysis during the extraction procedure. All isotopes we measured in seven cycles over a 50−55-minute period using peak-jumping mode. Identical analytical procedures as for samples were employed for blank and air calibration measurements, though monitors were heated using a resistance furnace. All isotopes were corrected for extraction line blanks, which contributed <5% of ^{38}Ar, $^{80,82}Kr$ and ^{128}Xe. Argon isotopes were corrected for instrument blank contribution, instrumental mass discrimination, radioactive decay of $^{37}Ar_{Ca}$ and $^{39}Ar_{K}$ and neutron-produced interference isotopes on ^{40}Ar, ^{39}Ar, ^{38}Ar and ^{36}Ar. Krypton and Xe were additionally corrected for epi-thermal neutron production using the scapolite monitor minerals BB1 and BB2/SP (Ruziè-Hamilton et al., 2016) and the Shallowater aubrite (Brazzle et al., 1999). The irradiation parameters are given in the **Table S-3**.

The halogen concentrations and element ratios of Bon Accord trevorite and bulk rock samples are presented in **Table S-3**. Potassium, Ca and Ba concentrations are also given. The halogen abundances of bulk Bon Accord are 182 ± 12 ppm Cl, 287 ± 6 ppb Br and 45 ± 5 ppb I, yielding Br/Cl and I/Cl ratios of 1.58 ± 0.17 ×10^{-3} and 2.47 ± 0.32 ×10^{-3} respectively. These concentrations are higher than detected in the trevorite separate, which give halogen abundances of 24 ± 1 ppm Cl, 7 ppb Br and 13 ± 1 ppb I, yielding Br/Cl and I/Cl ratios of 2.15 ± 0.24 × 10^{-3} and 3.67 ± 0.46 ×10^{-3}, respectively.

Noble Gas Analysis

The natural noble gas composition (He, Ne, Ar, Kr and Xe) of one 101.6 mg aliquot of bulk Bon Accord was determined using the custom-built 'Albatros' mass spectrometer at ETH Zürich. The isotope compositions and concentrations of all noble gases were measured in standard examinations (cf., Riebe et al., 2017) in a step at ~1700 °C. Typical blanks are (in 10^{-11} cm^3 STP): 0.003, 60, 6, 15, 4500, 0.36 and 0.43 for ^{3}He, ^{4}He (increased due to a short exposure of the gas to a pressure gauge mounted in glass), ^{20}Ne, ^{36}Ar, ^{40}Ar, ^{84}Kr and ^{132}Xe, respectively. Blank contributions to the total released gas are ~0.3% for ^{4}He %, 6-8 % for ^{3}He, $^{20-22}Ne$, ~3% for Ar and ~ 2% for Kr and Xe. The sample was fully degassed in the main temperature step as shown with a re-extraction step at slightly elevated temperature (~1750 °C).

Natural noble gas isotopic compositions and concentrations of the Bon Accord sample are presented in **Table S-4**. The light noble gases give R/R_a=1.60 ± 0.54 for He, the $^{20}Ne/^{22}Ne$ isotopic composition of approximately air (9.58 ± 0.20) and the $^{40}Ar/^{36}Ar$ ratio of 357 ± 14 is close to air with a radiogenic ^{40}Ar component. The heavy noble gases Kr and Xe are also air-like.

Chromium Isotope Analysis

Approximately 40 mg of whole rock powder was digested using concentrated HNO_3–HF–HCl acid mixtures. Chromium separation from Fe rich matrix requires three columns. The full methodology has previously been described in Bonnand et al. (2013; 2016), so only a brief summary is given here. The first column is designed to remove Fe from the sample. To this end, the column was filled with AG1 X8 resin and the sample loaded in 7 M HCl. The Fe sticks to the column whereas Cr is eluted. The second column is designed to isolate the Cr fraction from the main matrix cations (e.g., Ca, Na, Mg; see Bonnand et al., 2011). The Cr fraction and other minor elements such as Ti pass straight in the first elution of the second column procedure. In order to clean the Cr fraction from isobaric interferences (Ti, V and Fe) a third column chemistry was performed. The total

procedure yield for the three separations is ~75%. The total blank of this chemical process is ~0.2 ng, negligible compared to the 2000 ng processed through the columns.

The chromium isotope analysis of the Bon Accord sample was performed with a ThermoFisher Triton TIMS (Thermal Ionisation Mass Spectrometer) in static multicollection mode at the University of Oxford (UK). The chromium sample was loaded onto an outgassed zone refined Re filament in 1 µL 6 M HCl, along with 3 µL of a mixture of silicic and boric acids. The amplifier gains were performed daily. The baseline was measured after each block of 20 cycles, with amplifier rotation after each block. Samples and standards were run with a typical beam current of 6×10^{-11} A of ^{52}Cr for 27 blocks of 20 cycles. The integration time per cycle is 8.4 s. Interferences were monitored on ^{56}Fe, ^{49}Ti and ^{51}V, such that ^{54}Cr and ^{50}Cr signals were corrected for isobaric interferences. These corrections were always negligible. Chromium isotope ratios were corrected for mass fractionation using an exponential law and $^{50}Cr/^{52}Cr = 0.051859$ (Shields et al., 1966). The external reproducibility and accuracy of $\varepsilon^{53}Cr$ and $\varepsilon^{54}Cr$ were assessed by 2 standard deviation of NIST SRM 979 processed through chemical purification and are 0.00 ± 0.10 and 0.00 ± 0.19, respectively (2 s.d.; n = 15).

Laser Ablation ICP-MS HSE analysis

Compositions of Bon Accord materials were characterized for highly siderophile element (HSE) abundances using an Element 2 ICP-MS system to a New Wave Research UP213 Laser Ablation System at the University of Maryland. Ablation analysis took place in a 3 cm^3 ablation cell. The cell was flushed with a He-gas flow mixed with Ar as a carrier at ~ 1 l min^{-1}. Signals were acquired in Time Resolved Acquisition, devoting around 20 s for the blank and 40 s for measurement of the analyses. Wash time between each analysis was 120 s. The laser was fired using an energy density of ~3.4 J cm^{-2} at a frequency of 5 Hz and a beam size of 100 µm. Standardization was performed using iron meteorites Hoba, Filomena and Coahuila as certified reference material, using preferred values reported by Day et al. (2018) for the HSE, as well as USGS MRM Mass-1 Powder (CuFeZn sulfide). The isotopes of ^{99}Ru, ^{101}Ru, ^{102}Ru, ^{103}Rh, ^{105}Pd, ^{185}Re, ^{187}Os, ^{189}Os, ^{193}Ir, ^{195}Pt, were used for quantification. ^{34}S, ^{53}Cr, ^{57}Fe, ^{60}Ni, ^{25}Mg, ^{29}Si and ^{44}Cawere monitored to evaluate the ablation of any surrounding phases. External reproducibility for most of the highly siderophile and chalcophile element abundances is better than 5 to 10%. The isotopes ^{57}Fe or ^{60}Ni were used as the internal reference element using values of phases presented in **Table S-1**. Sensitivity tests were conducted during each analytical session, with limits of detection at 5 cps for the HSE, equating to ~0.03 ppm and a conservative limit of quantification of 0.06 ppm (see Paquet et al., 2021).

Bulk rock HSE and Re-Os isotope analysis

Osmium isotope and HSE abundance analyses of bulk rock powders measured for major and trace elements were performed at the SIGL. Approximately 100 mg of homogenized powder was precisely weighted before digestion in sealed borosilicate Carius tubes with isotopically enriched multi-element spikes (^{99}Ru, ^{106}Pd, ^{185}Re, ^{190}Os, ^{191}Ir, ^{194}Pt), and 7 ml of a 1:2 mixture of multiply Teflon distilled HCl and HNO_3 purged of excess Os by repeated treatment and reaction with H_2O_2. Samples were digested to a maximum temperature of 270˚C in an oven for 72 h. Osmium was triply extracted from the acid using CCl_4 and then back extracted into HBr, prior to purification by micro-distillation. Rhenium and the other HSE were recovered and purified from the residual solutions using standard anion exchange separation techniques (Day et al., 2016).

Isotopic compositions of Os were measured in negative-ion mode using a ThermoScientific Triton thermal ionization mass spectrometer in peak-jumping mode on the secondary electron multiplier. Rhenium, Pd, Pt, Ru and Ir were measured using a Cetac Aridus II desolvating nebuliser coupled to a ThermoScientific iCAPQc ICP-MS. Offline corrections for Os involved an oxide correction, an iterative fractionation correction using $^{192}Os/^{188}Os = 3.08271$ and assuming the exponential law, a ^{190}Os spike subtraction and an Os blank subtraction. Precision for $^{187}Os/^{188}Os$, determined by repeated measurement of the UMCP Johnson-Matthey standard during the analytical campaign was better than 0.2% (2 SD; 0.11373 ±7; n = 9). Rhenium, Ir, Pt, Pd and Ru isotopic ratios for sample solutions were corrected for mass fractionation using the deviation of the standard average run on the day over the natural ratio for the element. External reproducibility for HSE analyses was better than 0.5% for 0.5 ppb solutions and all reported values are blank corrected. The total procedural blank run with the samples gave $^{187}Os/^{188}Os = 0.206 \pm 0.006$, with

quantities (in picograms) of 0.3 [Re], 15 [Pd], 18 [Pt], 16 [Ru], 2 [Ir] and 0.3 [Os]. These blanks resulted in negligible corrections to samples in all cases (<0.1%).

A comparison of the mineral mapping, the LA-ICP-MS data, and the bulk HSE abundances indicates that the bulk rock HSE budget is controlled by the trevorite-hosted HSE-rich inclusion phases and does not seem to be affected by post-formation alteration.

Zinc Isotope Analysis

We employed methods for the purification and isotopic measurement of Zn described previously (e.g., Chen et al. 2013; van Kooten and Moynier, 2019; Day et al., 2022). Samples were dissolved in a 4:1 mixture of ultra-pure HF/HNO_3 in Teflon beakers for 96 h. Zinc purification was achieved using anion-exchange chromatography, with recovery of 99 ±1%. The samples were loaded in 1.5N HBr on 0.25 ml AG-1X8 (200-400 mesh) ion-exchange columns and Zn was collected in 0.5N HNO_3. The Zn fraction was further purified by eluting the samples twice on a 100 μl column, with the same eluting solutions. The blank measured with samples was 5 ng, and generally represents less than 1% of total measured Zn for most samples. Zinc isotopic compositions were measured on the ThermoElectron Neptune Plus multi collector-inductively coupled plasma-mass spectrometer housed at the Institute de Physique du Globe, Paris. The Faraday cups were positioned to collect the masses 62, 63, 64, 65, 66, 67 and 68. Possible ^{64}Ni isobaric interferences were controlled and corrected by measuring the intensity of the ^{62}Ni peak. A solution containing 500 ppb Zn in 0.1 M HNO_3 was prepared for isotopic analysis. Isotopic ratios of Zn in all samples were analyzed using a spray chamber combined with a 100 μl/min PFA nebulizer. One block of 30 ratios in which the integration time of 1 scan was 10 seconds, were measured for each sample. The background was corrected by subtracting the on-peak zero intensities from a blank solution. The instrumental mass bias was corrected by bracketing each of the samples with the standard (i.e., the JMC-Lyon standard). Values are reported as the $\delta^{66}Zn$, $\delta^{67}Zn$ and $\delta^{68}Zn$ values, which represent the permil deviation of the $^{x}Zn/^{64}Zn$ (x=66, 67 and 68) ratio from the JMC-Lyon standard. The error is represented by the external error as demonstrated in Chen et al. (2013) to be 0.04, 0.05 and 0.05 (2SD) for $\delta^{66}Zn$, $\delta^{67}Zn$ and $\delta^{68}Zn$, respectively.

Supplementary Tables

Table S-1 Nickel-rich minerals typical of the Bon Accord Ni oxide deposit.

Mineral	Generic Formula	Type	Description	Generic Composition (wt.%)							
				SiO_2	Al_2O_3	MgO	FeO	Fe_2O_3	NiO	H_2O	BO_5
Bonaccordite	Ni_2FeBO_5	Borate	Ni-rich borate					30.2	56.6		13.2
Liebenbergite	$(Ni,Mg)_2SiO_4$	Silicate	Ni-rich olivine	31.3		10.5			58.3		
Népouite	$Ni_3Si_2O_5(OH)_4$	Silicate	Ni-rich serpentine	31.6					59.9	9.5	
Nimite	$(Ni,Mg,Fe)_5Al(Si_3Al)O_{10}(OH)_8$	Silicate	Ni-rich phyllosilicate	27.0	15.3	10.3	3.2	4.8	29.0	10.4	
Trevorite	$NiFe_2O_4$	Oxide	Ni-rich spinel		<1.0	<1.0	9.3	68.5	21.3		

Table S-2a. Major element composition (wt.% oxide) of bulk Bon Accord and trevorite and silicate concentrates. Data are recalculated to a normalized anhydrous composition. An average bulk composition (n=2) with 2 standard deviation (S.D.) is calculated.

	SiO_2	TiO_2	$Al2O_3$	$FeO_{(t)}$	NiO	MnO	MgO	CaO	Na_2O	K_2O	P_2O_5
Trevorite	33.61	0.14	2.42	46.84	12.42	0.02	3.64	0.18	0.62	0.10	0.02
Silicate	58.41	0.03	4.69	10.01	19.17	0.02	6.84	0.20	0.55	0.09	
Bulk	39.46	0.11	7.09	28.25	14.98	0.03	9.13	0.00	0.88	0.07	
Bulk	42.60	0.10	6.90	27.00	13.59	0.02	8.58	0.03	1.07	0.10	
Average Bulk	41.03	0.10	7.00	27.63	14.28	0.00	8.85	0.00	0.97	0.09	
2 S.D.	*4.43*	*0.01*	*0.27*	*1.76*	*1.97*	*0.00*	*0.78*	*0.00*	*0.26*	*0.04*	

Table S-2b. Trace element composition (ppm) of bulk Bon Accord and trevorite and silicate concentrates measured by solution ICP-MS.

	Trevorite	Silicate	Bulk	Bulk
Li	0.92	1.29	2.17	1.71
B	3.69	2.93	3.97	3.00
Sc	1.70	3.08	3.97	3.01
V	30.1	4.5	23.7	19.0
Cr	709	381	972	792
Co	2780	3399	4006	3171
Cu	6.6	5.2	10.6	7.6
Zn	32.7	49.7	55.9	43.5
Ga	76.3	40.1	88.7	72.2
Ge	65.7	38.0	60.2	49.9
Se	0.15	0.36	0.13	0.08
Rb	0.40	0.12	0.92	0.77
Sr	1.09	0.30	1.67	1.21
Y	4.34	1.48	3.96	3.26
Zr	28.9	47.8	80.4	65.2
Nb	1.28	0.48	1.38	1.13
Mo	0.20	0.07	0.15	0.13
Sn	10.48	2.14	8.16	6.82
Te	0.02	0.01	0.02	0.01
Cs	0.04	0.06	0.11	0.08
Ba	1.53	7.05	15.27	3.73
La	1.08	0.29	1.35	1.19
Ce	2.66	0.65	3.05	2.69
Pr	0.31	0.08	0.35	0.31
Nd	1.37	0.34	1.44	1.27
Sm	0.39	0.10	0.36	0.31
Eu	0.03	0.01	0.04	0.03
Gd	0.497	0.135	0.450	0.372
Tb	0.095	0.027	0.083	0.068
Dy	0.695	0.197	0.591	0.488
Ho	0.158	0.046	0.137	0.109
Er	0.481	0.141	0.415	0.339
Tm	0.077	0.023	0.065	0.054
Yb	0.514	0.168	0.449	0.368
Lu	0.075	0.027	0.070	0.058
Hf	0.55	0.90	1.57	1.27
Ta	0.08	0.04	0.10	0.07
W	0.23	0.07	0.19	0.16
Ir	0.17	0.09	0.13	0.10
Au	0.40	0.21	0.54	0.36
Tl	0.11	0.04	0.28	0.25
Pb	0.59	0.14	0.81	0.65
Th	0.47	0.14	0.59	0.45
U	0.13	0.08	0.18	0.14

Table S-3. Potassium, Ca, Ba and halogen abundances in Bon Accord trevorite (12.2 mg) and bulk rock (5.1 mg) determined by NI-NGMS. Potassium, Ca, Ba and Cl are given in ppm and Br and I are given in ppb. All ratios are by weight. Uncertainties are 1σ, and are given in the units of the last significant figure(s).

	K (ppm)	Ca (ppm)	Cl (ppm)	Br (ppb)	I (ppb)	Ba (ppm)	K/Cl (wt.)	Br/Cl ($\times 10^{-3}$ wt.)	I/Cl ($\times 10^{-3}$ wt.)
Bulk	548 (26)	8600 (300)	125 (9)	287 (26)	45 (5)	17 (2)	3.0 (2)	1.58 (17)	0.25 (3)
Trevorite	103 (4)	830 (130)	24 (1)	74 (7)	13 (1)	4 (1)	2.9 (1)	2.15 (24)	0.37 (5)

Irradiation parameters and correction factors: J-value: 0.00625 ± 0.00005. Estimated thermal & epi-thermal neutron fluxes: ~6.2 x 10^{18} n cm^{-2} and ~1.6 x 10^{17} n cm^2. Alpha: 0.42 ± 0.02 Beta: 9.0 ± 0.5 $^{40}Ar/^{39}Ar_K$: 0.114 $^{38}Ar/^{39}Ar_K$: 0.0121 $^{36}Ar/^{37}Ar_{Ca}$: 0.000297 $^{39}Ar/^{37}Ar_{Ca}$: 0.000727 $^{40}Ar/^{36}Ar$: 298.56 ± 0.31 (Lee et al. 2006)

Table S-4. Noble gas data for a 101.60 mg sample of Bon Accord. Uncertainties are 1σ, and are given in the units of the last significant figure(s). Helium, Ne and Ar concentrations are units of 10^{-8} cm^3 STP g^{-1} and Kr and Xe are in units of 10^{-10} cm^3 STP g^{-1}.

^{3}He	^{4}He	^{3}He/^{4}He ($\times 10^4$)	R/R_a	^{20}Ne	^{20}Ne/^{22}Ne	^{21}Ne/^{22}Ne		
0.01035 (74)	4637 (100)	0.0223 (17)	1.60 (12)	0.54 (2)	9.58 (20)	0.045 (2)		
^{36}Ar	^{40}Ar	^{36}Ar/^{38}Ar	^{40}Ar/^{36}Ar					
2.983 (71)	1064 (48)	5.26 (7)	357 (14)					
^{84}Kr	^{74}Kr/^{84}Kr	^{80}Kr/^{84}Kr	^{82}Kr/^{84}Kr	^{83}Kr/^{84}Kr	^{86}Kr/^{84}Kr			
13.7 (2)	0.00612 (12)	0.0399 (6)	0.2020 (28)	0.1985 (27)	0.3035 (42)			
^{132}Xe	^{124}Xe/^{132}Xe	^{126}Xe/^{132}Xe	^{128}Xe/^{132}Xe	^{129}Xe/^{132}Xe	^{130}Xe/^{132}Xe	^{131}Xe/^{132}Xe	^{134}Xe/^{132}Xe	^{136}Xe/^{132}Xe
1.91 (3)	0.00356 (13)	0.0035 (1)	0.072 (1)	0.98 (2)	0.15 (3)	0.79 (1)	0.389 (7)	0.331 (9)

Table S-5. Highly-siderophile element (HSE) abundance data are given in ppm. $^{187}Re/^{188}Os$ and $^{187}Os/^{188}Os$ data have a 2 standard error (S.E.). LA is LA-ICP-MS and ID is isotope dilution (bulk rock).

	Os	Ir	Ru	Rh	Pt	Pd	Re	$^{187}Re/^{188}Os$	± 2S.E.	$^{187}Os/^{188}Os$	± 2S.E.
Ni-Rich Sulfide (LA)	BDL	BDL	2.5	0.4	BDL	BDL	BDL				
Ni-Rich Sulfide (LA)	0.4	2.4	14	1.0	13	3.8	1.6				
Ni-Rich Sulfide (LA)	BDL	0.8	8.0	BDL	4.6	8.0	0.1				
Ni-Rich Serpent. (LA)	0.1	0.1	0.1	BDL	BDL	0.4	0.2				
Trevorite (LA)	0.6	0.8	0.7	BDL	1.7	0.1	0.4				
Trevorite (LA)	1.2	1.0	2.3	0.1	3.8	0.3	0.4				
Trevorite (LA)	0.5	0.4	0.9	0.1	1.6	0.3	0.3				
Trevorite (LA)	1.0	0.6	1.2	0.2	1.0	0.6	0.2				
Trevorite (LA)	1.1	0.6	2.3	0.4	3.1	0.1	0.3				
Trevorite (LA)	0.6	0.1	0.5	0.3	0.5	BDL	0.1				
Trevorite (LA)	0.9	1.0	2.4	0.2	3.1	0.6	0.5				
Trevorite (LA)	1.6	1.1	1.6	0.1	10	1.1	0.1				
Trevorite (ID)	0.309	0.267	1.086	ND	1.632	0.709	0.122	1.921	0.211	0.21265	0.00024
Silicate (ID)	0.124	0.142	0.576	ND	0.822	0.992	0.033	1.290	0.103	0.18261	0.00009
Bulk Rock (ID)	0.196	0.178	0.777	ND	1.083	0.806	0.070	1.745	0.201	0.20304	0.00014
Bulk Rock (ID)	0.196	0.180	0.741	ND	1.116	0.801	0.070	1.746	0.201	0.20364	0.00014

Table S-6. Zinc isotopic data for three Bon Accord (bulk) samples.

Sample	Zn (ppm)	$\delta^{66}Zn$	$\delta^{67}Zn$	$\delta^{68}Zn$
BA_1	28.3	0.42	0.61	0.82
BA_2	28.5	0.52	0.77	1.02
BA_3	28.7	0.55	0.84	1.10

Table S-7 Serpentinization and desulfurization reaction parameters and mass balance for the Bon Accord Ni oxide deposit

		Reactants			Products		
Species	$Fe_3Ni_6S_8$	FeS_2	FeS	H_2O	$NiFe_2O_4$	H_2S	H_2
Molecular Weight							
Reaction Quantity	1	3	6	24	6	20	4
Determination	Calc.	Calc.	Calc.	Calc.	Fixed*	Calc.	Calc.
kg	6,930	3,220	4,730	1,160	12,600	6,110	72
tonnes	6.9	3.2	4.7	1.2	12.6	6.1	0.1

**The amount of trevorite is fixed by the modal proportion of trevorite and the excavated volume of the Bon Accord body. Calc. = calculated quantities based on the reaction stoichiometry and fixed amount of trevorite. Reaction quantities represent a minimum value, reflecting the known extent of the excavated Bon Accord body (Tredoux et al., 1989).*

Supplementary Figures

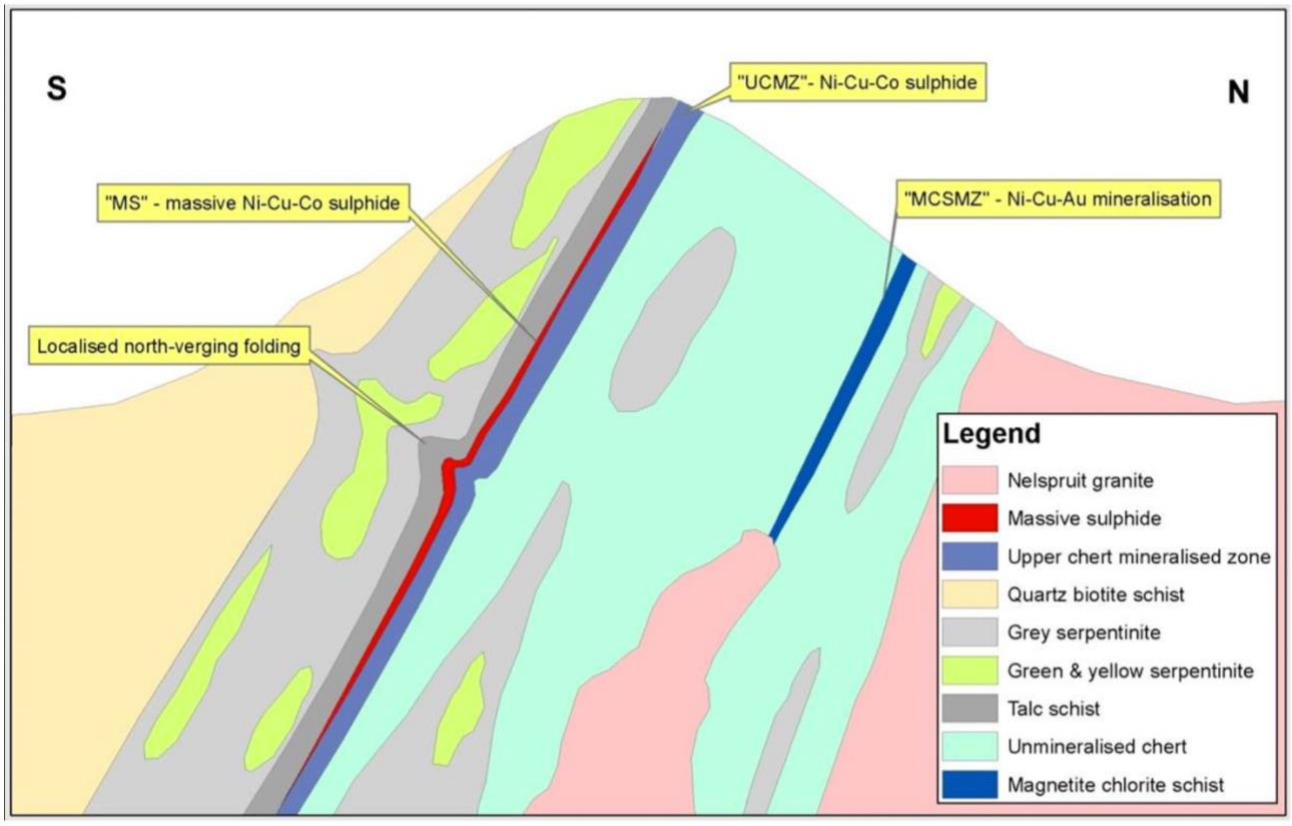

Figure S-1. Schematic (not to scale) north-south oriented cross section through the stratigraphy ~1 km southeast of the Bon Accord Ni-oxide deposit, which was sited at the same location in the sequence as the trevorite-nimite schists in the hanging wall immediately above the Ni-sulfide mineralization (shown in red). See **Figure 1 (main manuscript)** for *approximate* line of section (S-N). This cross-section cartoon is taken and adapted from Hornsey et al. (2009).

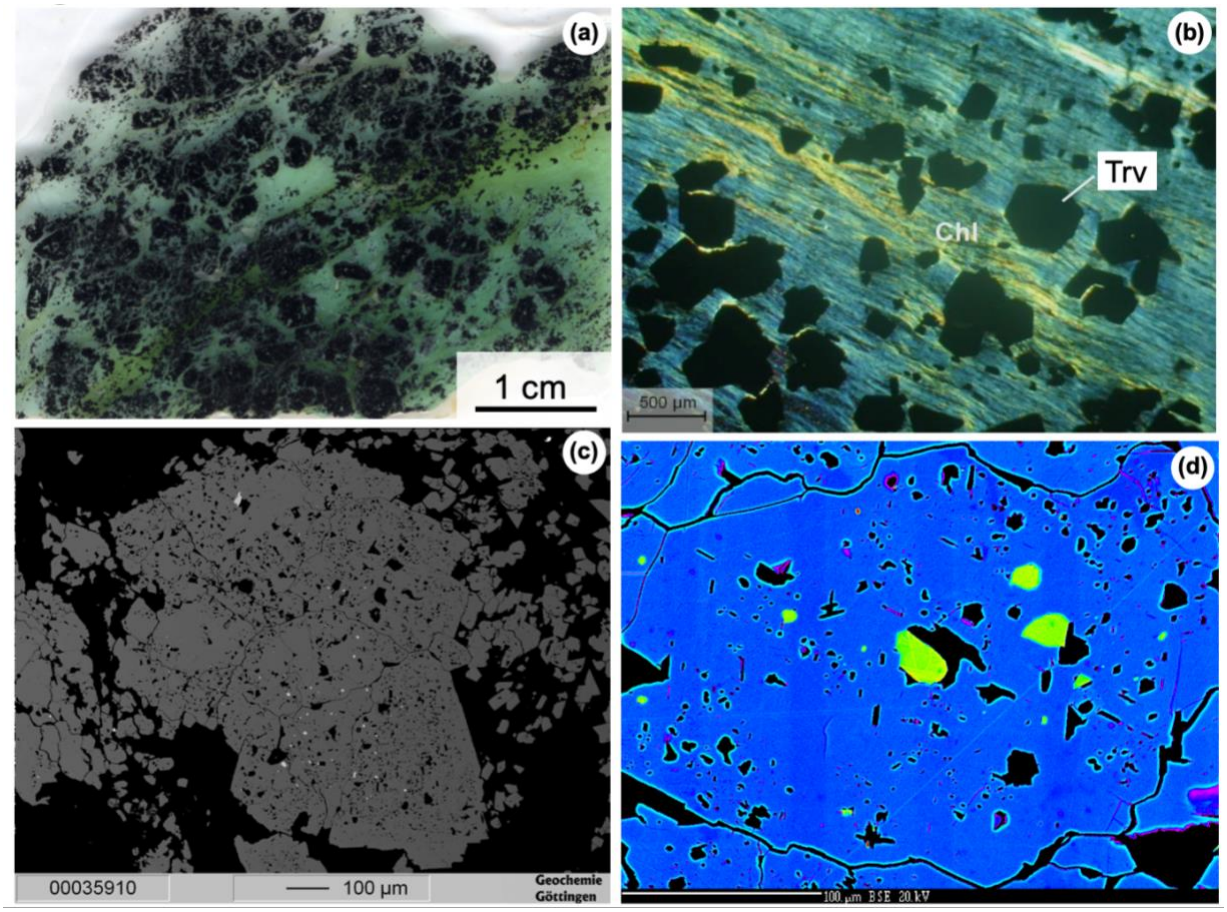

Figure S-2. Mineralogy and microstructure of the Bon Accord trevorite deposit. (a) Thin section scan of the Bon Accord Ni-deposit, showing the abundance and distribution of trevorite (opaque phase) in the sample. The green-colored groundmass is comprised of Ni-serpentine (népouite) and Ni-chlorite (nimite). (b) Crossed polarized light image of trevorite-bearing chlorite schist, sampled ~1 km southeast of the Bon Accord Ni oxide deposit locality (see also Hornsey et al., 2009). Chl = Ni-chlorite/nimite; Trv = trevorite. (c) Backscattered electron micrograph of a trevorite aggregate, containing abundant Ni-sulfide and Ni-arsenide inclusions (bright phases). (d) False-coloured backscattered electron micrograph of sulfide inclusions (green) in trevorite (blue). Note that (c) and (d) were collected in the analytical campaign of O'Driscoll et al. (2014).

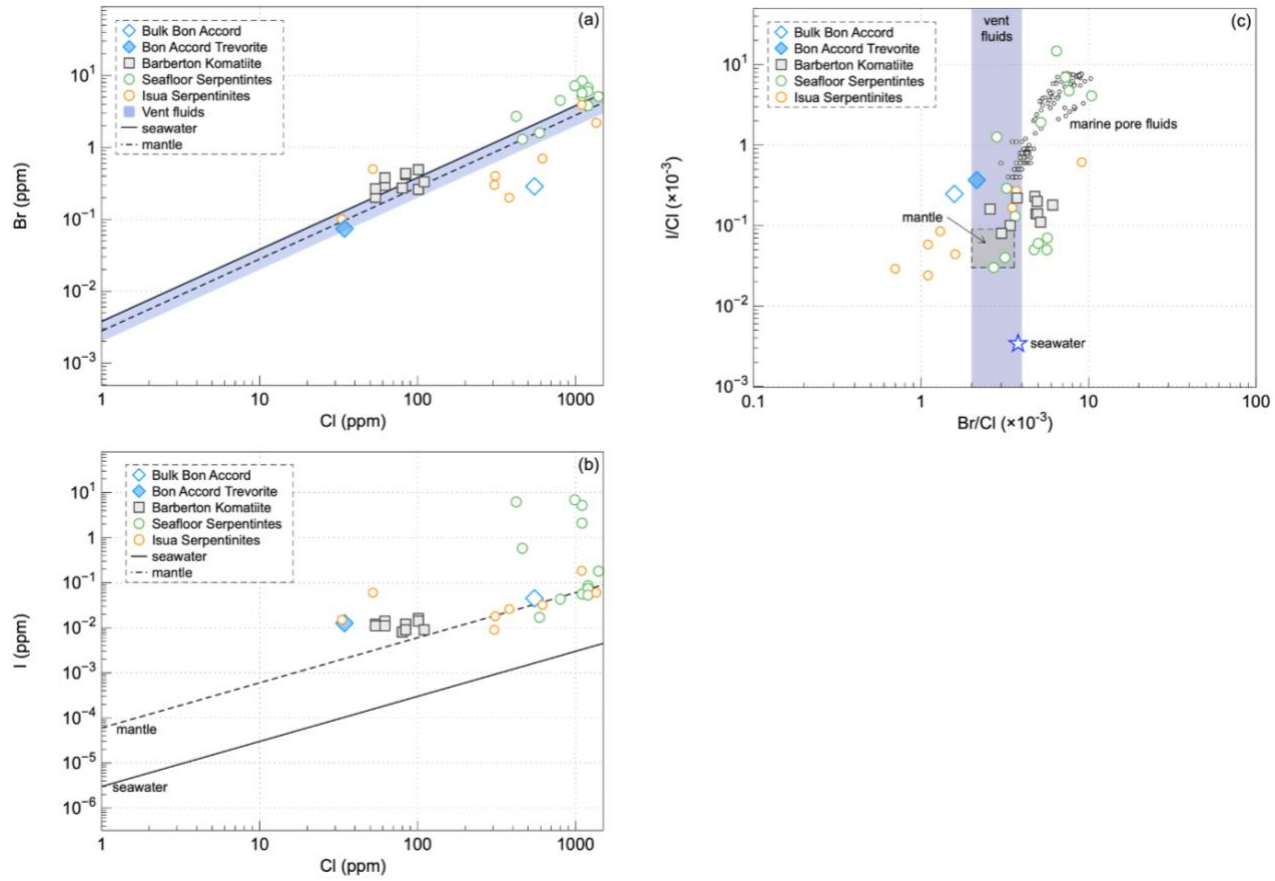

Figure S-3. Br/Cl and I/Cl ratios of Bon Accord in relation to reference compositions for modern seawater and fields for komatiites, serpentinites, marine pore fluids, mantle and modern hydrothermal vent fluids (Br/Cl range only shown in vertical band in (c)). (Reference data sources: D'Andres et al., 2019; Kendrick et al., 2012; 2013; 2014; Kastner et al., 1990; Muramatsu et al., 2007.)

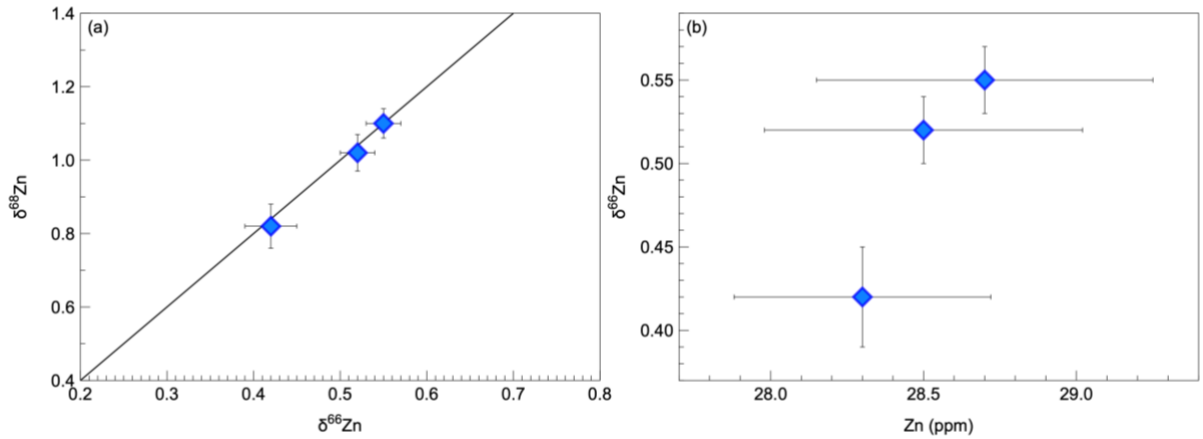

Figure S-4. Bon Accord zinc isotope systematics (a) $\delta^{68}Zn$ versus $\delta^{66}Zn$ and $\delta^{66}Zn$ versus Zn abundance (ppm) in three samples of bulk Bon Accord material. The solid line in (a) represents a slope of two for mass-dependent mass-fractionation.

Supplementary References

Anhaeusser, C.R., 1986, Archaean gold mineralization in the Barberton Mountain Land, *in* Anhaeusser, C.R., Maske, S., eds., Mineral Deposits of Southern Africa: Geological Society of South Africa, Johannesburg, South Africa, v. 1, p. 113-154.

Anhaeusser, C.R., 2019, The geology and tectonic evolution of the northwest part of the Barberton Greenstone Belt, South Africa: A review: South African Journal of Geology, v. 122(4), p. 1-34.

Bonnand, P., Parkinson, I.J., James, R.H., Karjalainen, A.-M., and Fehr, M.A., 2011, Accurate and precise determination of stable Cr isotope compositions in carbonates by double spike MC-ICP-MS: Journal of Analytical Atomic Spectrometry, v. 26, p. 528-535.

Bonnand, P., James, R.H., Parkinson, I.J., Connelly, D.P., and Fairchild, I.J., 2013, The chromium isotopic composition of seawater and marine carbonates: Earth and Planetary Science Letters, v. 382 (2013), p. 10-20.

Bonnand, P., Williams, H.M., Parkinson, I.J., Wood, B.J., and Halliday A.N., 2016, Stable chromium isotopic composition of meteorites and metal-silicate experiments: Implications for fractionation during core formation: Earth and Planetary Science Letters, v. 3, p. 4-7.

Brazzle, R.H., Pravdivtseva, O.V., Meshik, A.P., and Hohenberg, C.M., 1999, Verification and interpretation of the I-Xe chronometer: Geochimica et Cosmochimica Acta, v. 63, p. 739-760.

Chen, H., Savage, P.S., Teng, F.-Z., Helz, R.T., and Moynier, F., 2013, Zinc isotope fractionation during magmatic differentiation and the isotopic composition of the bulk Earth: Earth and Planetary Science Letters v. 369-370, p. 32-42.

D'Andres, J., Kendrick, M.A., Bennett, V.C., and Nutman, A.P., 2019, Halogens in serpentinites from the Isua supracrustal belt, Greenland: An Eoarchean seawater signature and biomass proxy?: Geochimica et Cosmochimica Acta, v. 262, p. 31-59.

Day, J.M.D., Tait, K. T., Udry, A., Moynier, F., Liu, Y., and Neal, C. R., 2018, Martian magmatism from plume metasomatized mantle: Nature Communications, v. 9(1), p. 1-8.

Day, J.M.D., Maria-Benavides, J., McCubbin, F.M., and Zeigler, R.A., 2018, The potential for metal contamination during Apollo lunar sample curation: Meteoritics and Planetary Sciences, v. 53, p. 1283-1291.

Day, J. M. D., Waters, C. L., Schaefer, B. F., Walker, R. J., and Turner, S., 2016, Use of hydrofluoric acid desilicification in the determination of highly siderophile element abundances and Re-Pt-Os isotope systematics in mafic-ultramafic rocks: Geostandards and Geoanalytical Research, v. 40, p. 49-65.

Day, J. M. D., Moynier, F., and Ishizuka, O., 2022, A partial melting control on the Zn isotope composition of basalts: Geochemical Perspectives Letters, v. 23, p. 11-16.

Dziggel, A., Poujol, M., Otto, A., Kisters, A.F.M., Trieloff, M., Schwarz, W.H., and Meyer, F.M., 2010, New U-Pb and $^{40}Ar/^{39}Ar$ ages from the northern margin of the Barberton Greenstone Belt, South Africa: Implications for the formation of Mesoarchaean gold deposits: Precambrian Research, v. 179, p. 206-220.

Hornsey, R., and Chunnett, I., 2009, The Bon Accord Ni-sulphide deposit – Ni-sulphide mineralization within the 3.5 Ga Barberton Greenstone Belt, South Africa: International Ni-Cu(Pt) Deposit Symposium, Xi'an, China, Published Abstract.

Kastner, M., Elderfield, H., Martin, J. B., Suess, E., Kvenvolden, K. A., and Garrison, R. E., 1990, Diagenesis and interstitial-water chemistry at the Peruvian continental margin-major constituents and strontium isotopes, *in* Suess, E. et al., eds., Proceedings of the Ocean Drilling Program Scientific Results: College Station, Texas: Ocean Drilling Program, v. 112, p. 413-440.

Keenan, J., 1986, The Bon Accord nickel sulphide deposit, Barberton Greenstone Belt, *in* Anhaeusser, C.R., Maske, S., eds., Mineral Deposits of Southern Africa: Geological Society of South Africa, Johannesburg, South Africa, v. 1., p. 281-286.

Kendrick, M. A., Kamenetsky, V. S., Phillips, D., and Honda, M., 2012, Halogen systematics (Cl, Br, I) in mid-ocean ridge basalts: a Macquarie Island case study: Geochimica et Cosmochimica Acta, v. 81, p. 82-93.

Kendrick, M. A., Honda, M., Pettke, T., Scambelluri, M., Phillips, D., and Giuliani, A., 2013, Subduction zone fluxes of halogens and noble gases in seafloor and forearc serpentinites: Earth and Planetary Science Letters, v. 365, p. 86-96.

Kendrick, M. A., Jackson, M. G., Kent, A. J., Hauri, E. H., Wallace, P. J., and Woodhead, J., 2014, Contrasting behaviours of CO_2, S, H_2O and halogens (F, Cl, Br, and I) in enriched-mantle melts from Pitcairn and Society seamounts: Chemical Geology, v. 370, p. 69-81.

Lowe, D.R., 1999, Geologic evolution of the Barberton Greenstone Belt and vicinity, *in* Geologic Evolution of the Barberton Greenstone Belt, South Africa, Lowe, D.R., Byerly, G.R., eds., Geological Society of America Special Paper 329, p. 287-312.

Muramatsu, Y., Doi, T., Tomaru, H., Fehn, U., Takeuchi, R., Matsumoto, R., 2007, Halogen concentrations in pore waters and sediments of the Nankai trough, Japan: Implications for the origin of gas hydrates: Applied Geochemistry, v. 22(3), p. 534-556.

O'Driscoll, B., Clay, P.L., Lenaz, D., Cawthorn, R.G., Adetunji, J., and Kronz, A., 2014, Trevorite: Ni-rich spinel formed by metasomatism and desulphurization processes at Bon Accord, South Africa?: Mineralogical Magazine, v. 78, p. 145-163.

Paquet, M., Day, J.M.D., Udry, A., Hattingh, R., Kumler, B., Rahib, R.R., Tait, K.T., Neal, C.R., 2021, Highly siderophile elements in shergottite sulfides and the sulfur content of the martian mantle: Geochimica et Cosmochimica Acta, v. 293, p. 379-398.

Renne, P.R., Mundil, R., Balco, G., Min, K., and Ludwig, K.R., 2010, Joint determination of ^{40}K decay constants and $^{40}Ar^*/^{40}K$ for the Fish Canyon sanidine standard, and improved accuracy for $^{40}Ar/^{39}Ar$ geochronology: Geochimica et Cosmochimica Acta, v. 74, p. 5349-5367.

Riebe, M.E.I., Welten, K.C., Meier, M.M.M., Wieler, R., Barth, M.I.F., Ward, D., Bischoff, A., Caffee, M.W., Nishiizumi K., and Busemann, H., 2017, Cosmic-ray exposure ages of six chondritic Almahata Sitta fragments: Meteoritics and Planetary Science, v. 52, p. 2353-2374.

Ruzié-Hamilton, L., Clay, P.L., Burgess, R., Joachim, B., Ballentine, C.J., and Turner, G., 2016, Determination of halogen abundances in terrestrial and extraterrestrial samples by the analysis of noble gases produced by neutron irradiation: Chemical Geology, v. 437, p. 77-87.

Shields, W.R., Murphy, T.J., Catanzar, E.J., and Garner E.L., 1966, Absolute isotopic abundance ratios and atomic weight of a reference sample of chromium: Journal of Research of the National Bureau of Standards. Section A, Physics and Chemistry, v. 70, p. 193-197.

Tredoux, M., de Wit, M.J., Hart, R.J., Armstrong, R.A., Lindsay, N.M., and Sellschop, J.P.F., 1989, Platinum group elements in a 3.5 Ga nickel-iron occurrence: Possible evidence of a deep mantle origin: Journal of Geophysical Research, v. 94(B1), p. 795-813.

Trevor, T.G., 1920, Nickel: Notes on the occurrence in the Barberton district: South African Journal of Industry, v. 3, p. 532-533.

van Kooten, E., and Moynier, F., 2019, Zinc isotope analyses of singularly small samples (<5 ng Zn): Investigating chondrule-matrix complementarity in Leoville: Geochimica et Cosmochimica Acta, v. 261, p. 248-268.

Viljoen, M.J., Viljoen, R.P., 1969, An introduction to the geology of the Barberton granite-greenstone terrain: Geological Society of South Africa Special Publication, v. 2, p. 9-28.